Biosensors and Bioelectronics 52 (2014) 1–7

Contents lists available at ScienceDirect

Biosensors and Bioelectronics

journal homepage: www.elsevier.com/locate/bios

Preparation and characterization of three dimensional graphene foam supported platinum–ruthenium bimetallic nanocatalysts for hydrogen peroxide based electrochemical biosensors

Chih-Chien Kung [a,*], Po-Yuan Lin [b], Frederick John Buse [c], Yuhua Xue [d], Xiong Yu [e], Liming Dai [d], Chung-Chiun Liu [a]

[a] Department of Chemical Engineering, Case Western Reserve University, 10900 Euclid Avenue, Cleveland, OH 44106, USA
[b] Department of Materials Science and Engineering, Case Western Reserve University, Cleveland, OH 44106, USA
[c] Mentor High School, Mentor, OH 44060, USA
[d] Department of Macromolecular Science and Engineering, Case Western Reserve University, Cleveland, OH 44106, USA
[e] Department of Civil Engineering, Case Western Reserve University, Cleveland, OH 44106, USA

ARTICLE INFO

Article history:
Received 30 May 2013
Received in revised form
2 August 2013
Accepted 15 August 2013
Available online 27 August 2013

Keywords:
PtRu bimetallic nanoparticles
Nanocatalysts
Carbon supported materials
H_2O_2 detection
3D graphene foam (GF)

ABSTRACT

The large surface, the excellent dispersion and the high degrees of sensitivity of bimetallic nanocatalysts were the attractive features of this investigation. Graphene foam (GF) was a three dimensional (3D) porous architecture consisting of extremely large surface and high conductive pathways. In this study, 3D GF was used incorporating platinum–ruthenium (PtRu) bimetallic nanoparticles as an electrochemical nanocatalyst for the detection of hydrogen peroxide (H_2O_2). PtRu/3D GF nanocatalyst exhibited a remarkable performance toward electrochemical oxidation of H_2O_2 without any additional mediator showing a high sensitivity (1023.1 $\mu A\ mM^{-1}\ cm^{-2}$) and a low detection limit (0.04 μM) for H_2O_2. Amperometric results demonstrated that GF provided a promising platform for the development of electrochemical sensors in biosensing and PtRu/3D GF nanocatalyst possessed the excellent catalytic activity toward the H_2O_2 detection. A small particle size and a high degree of the dispersion in obtaining of large active surface area were important for the nanocatalyst for the best H_2O_2 detection in biosensing. Moreover, potential interference by ascorbic acid and uric acid appeared to be negligible.

1. Introduction

Electrochemical biosensors based on the enzymatic activity received significant interest in recent years. The advantages of the electrochemical biosensors included low cost, portability, a fast response time, and ease-of-usage by non-specialist personnel (Chen et al., 2012a). Hydrogen peroxide (H_2O_2) was an electrochemical active species produced by many oxidase enzymes. Thus, the measurement of H_2O_2 in various enzymatic reactions could quantify the analyte for biomarker detections as shown in Eq. (1) (Guascito et al., 2008). The use of electrode or catalyst-modified electrode as a transducer was based on Eq. (2) of H_2O_2 oxidation:

$$\text{analyte} + O_2 \overset{\text{oxidase}}{\Longrightarrow} \text{byproduct} + H_2O_2 \quad (1)$$

$$H_2O_2 \overset{\text{electrode}}{\Longrightarrow} O_2 + 2H^+ + 2e^- \quad (2)$$

The oxidation current of H_2O_2 was measured under a suitable applied potential between −0.1 V and +0.8 V. The changes in the concentration of the H_2O_2 were then related to the analyte concentration as shown in Eq. (1).

Transition metal nanoparticles were used in the development of electrochemical sensors and biosensors based on their catalytic activity (Gong et al., 2007; Privett et al., 2008). The large surface-to-volume ratio and special binding site on the surface of nanoparticles led to a fast communication between an enzymatic process and a nanoparticle response for signal transduction in biosensing or for catalytic reactions (Chakraborty and Raj, 2009). Pt nanoparticles were used in electrochemical detections based on its activity for the oxidation of H_2O_2 (Karam and Halaoui, 2008; McLamore et al., 2011; Shi et al., 2011). Electrodes modified with Pt nanoparticles enhanced electron transfer and reduced the overpotential for H_2O_2 oxidation (Evans et al., 2002; You et al., 2012). However, electrodes modified with pure Pt nanoparticles still required ca. +0.7 V versus Ag/AgCl to generate the oxidation current of H_2O_2. This high overpotential would oxidize ascorbic acid (AA) and uric acid (UA) in human blood resulting in an interference of the detection of the analyte (Chen et al., 2012b).

* Corresponding author. Tel.: +1 440 317 2816; fax: +1 216 368 8738.
E-mail address: cxk215@case.edu (C.-C. Kung).

0956-5663/$ - see front matter © 2013 Elsevier B.V. All rights reserved.
http://dx.doi.org/10.1016/j.bios.2013.08.025

Bimetallic nanoparticles created functional hybrid nanostructures, resulting in the variations in electronic, catalytic, or photonic property. The addition of a second metal contributed to the alterations in particle size, shape, surface-morphology, composition, chemical and physical properties including the catalytic activity and chemical selectivity of the material as compared to the single metallic nanocatalyst (Alayoglu et al., 2008). Specifically, among platinum based bimetallic nanocatalysts, PtRu nanocatalysts exhibited a superior activity in H_2O_2 detection. Several groups demonstrated that Ru required less activation energy than Pt in adsorbing OH_{ads} or O_{ads} (Kua and Goddard, 1999; Ge et al., 2001; Bligaard et al., 2004; Greeley et al., 2007; Lischka et al., 2007). Gsell et al. reported that the oxygen adsorption preferably occurred onto the Ru (0001), hexagonal close-packed (hcp), surface (Gsell et al., 1998; Jakob et al., 2001). This allowed the O_{ads} inhibitor to adsorb on Pt surface, thereby minimizing the surface "poisons" on the Pt metal. Consequently, Pt active binding sites were able to interact with H_2O_2, enhancing the catalytic activity of the H_2O_2 detection. The addition of promoters, including of adding a metallic third element, adjustment of preparation parameters, using of alterative supports, and heat treatments on the bimetallic nanocatalyst, was proposed (Prabhuram et al., 2006; Chang et al., 2009; Liu et al., 2011; Wei et al., 2011). Carbon powder, carbon nanotube (CNT), and graphene as the supporting materials for bimetallic nanocatalysts were used due to their unique structural, electrical, and mechanical properties (Prabhuram et al., 2006; Shi et al., 2012).

Carbon nanomaterials possessed unusual size-/surface-dependent properties (e.g., morphological, electrical, optical, and mechanical) which were useful in enhancing energy conversion and storage performance (Liu et al., 2008; Guo et al., 2008; Rolison et al., 2009; Dai et al., 2012). Specially, carbon materials enhanced the availability electrochemical active surface area (ECSA) of electrocatalyst providing high mass transport of reactants to the electrocatalyst. Carbon materials came in many forms and were often categorized by their dimensionality, such as zero dimensional (0D) fullerene, one dimensional (1D) CNT, and two dimensional (2D) graphene. Graphene possessed much more novel properties compared with fullerene and CNT (Mattevi et al., 2009; Loh et al., 2010; Wu et al., 2010). Graphene was a two dimensional monolayers of carbon atoms with high surface area, chemical stability, and thermal stability, making it as a useful growth substrate for energy conversion and electronics (Sundaram et al., 2011; Wang et al., 2011). However, graphene showed poor electrical conductivity and large resistance from structural defects (Bi et al., 2011; Chen et al., 2011). In order to overcome these shortcomings, a new strategy was proposed to grow graphene on three dimensional (3D) skeletons (graphene foam/porous graphene) with a large surface area (Lee et al., 2010; Yin et al., 2011). Graphene foam (GF) was a 3D multilayer freestanding and monolithic electrochemical graphene film which was a promising material using in chemical sensing and energy storage. This porous architecture of GF held extremely large surface and highly conductive pathways (Huang et al., 2012; Singh et al., 2013). GF also used as the freestanding electrode with a low resistance enhancing the mobility of charge carries based on its mechanical strength and continuous skeleton (Si et al., 2013).

In this study, the preparation of novel 3D GF using Ni foam as a sacrificial template in a facile process was described. The results of PtRu bimetallic nanocatalysts with various carbon substrate materials, such as Vulcan XC-72 carbon, graphene, and GF, as the supporting materials toward the H_2O_2 detection were investigated. The atomic structures of different carbon supports and the electroactivity of PtRu nanocatalysts were characterized by X-ray diffractometer (XRD), scanning electron microscopy (SEM), scanning transmission electron microscopy (STEM), and cyclic voltammetry (CV). The electrochemical measurements showed that the GF supported PtRu exhibited an excellent electrocatalytic activity toward the H_2O_2 detection. 3D PtRu/GF nanocatalyst also exhibited a superior conductivity, low detection limit and high sensitivity, providing a new opportunity for the design and application of electrode materials with enhanced performance in biosensing.

2. Experimental

2.1. Materials

Hydrogen hexachloroplatinate(IV) hexahydrate ($H_2PtCl_6 \cdot 6H_2O$, 37.5% Pt basis), ruthenium(III) chloride hydrate ($RuCl_3 \cdot nH_2O$, 99.8% purity), citric acid (99.5 wt.%) and sodium borohydride ($NaBH_4$, 99 wt.%) were purchased from Sigma Aldrich (St. Louis, MO). Nafion solution (LIQUION) was obtained from Ion Power Inc (New Castle, DE). Vulcan XC-72R carbon and graphene nanopowder (12 nm flakes) were received from Cabot Corporation (Boston, MA) and Graphene Supermarket (Calverton, NY), respectively. Phosphate buffer solution (PBS) (0.1 M) of pH 7.4 solution was prepared with 0.15 M KCl as the supporting electrolyte, KH_2PO_4, K_2HPO_4, and deionized water in appropriate portions.

2.2. Growth of the 3D graphene foam

3D GF was prepared as follows. A nickel foam (INCO, Alantum Advanced Technology Materials (Dalian) Co., Ltd., Dalian, Liaoning; pore size: 590 μm) was first heated up to 1000 °C in a horizontal quartz tube under Ar (500 sccm) and H_2 (200 sccm) and kept in situ for 5 min cleaning its surface and removing any thin surface oxide layer. CH_4 (5 sccm) was then introduced into the furnace tube for 5 min. At this stage, graphene coated nickel foam was formed. Upon cooling to room temperature (20 °C), the Ni foam covered with graphene was removed from the furnace tube and dip-coated with a poly(methyl methacrylate) (PMMA) solution (6 M in toluene), and then dried at 180 °C for 30 min forming a thin PMMA film on graphene surface (PMMA/GF@Ni) preventing structural failure of the resultant GFs when the nickel template was etched. The nickel foam was removed by immersing the whole structure in a HCl (3 M) solution at 70 °C for 5 h in order to obtain PMMA/GF. Finally, freestanding GF was obtained by dissolving the PMMA protection layer in hot acetone at 55 °C. The 3D GF then was used as the substrate for the adsorption of PtRu nanoparticles to synthesize PtRu/3D GF nanocatalyst.

2.3. Synthesis and modification of PtRu nanoparticle catalyst

The PtRu was synthesized using the borohydride reduction. Typically, in an experimental trail, the Pt and Ru precursors were first dissolved in deionized (DI) water achieving a 1.8 mM metal solution, respectively. Citric acid was used as the capping agent adding into the metal solution preventing nanoparticles agglomeration at a molar ratio of 0.42 between citric acid and the metal solution. The bimetallic PtRu solution was then adjusted to pH = 7.0 using 0.1 M NaOH solution and $NaBH_4$ was used as reducing agent and added dropwise into the metal solution. The amount of $NaBH_4$ was 1.4-times the molarity of PtRu which reduced the PtRu metal in the solution. The solution was stirred for 12 h at room temperature for the completion of the chemical reduction. For the preparation of PtRu nanocatalysts with carbon supported materials, the PtRu solution was first sonicated for 2 h and then mixed with 47.7 mg of various carbon supported materials, respectively. The nanocatalyst solution was stirred for 12 h at room temperature again. The nanocatalyst solution was thereafter washed with acetone three times and collected by centrifugation at 18,000 rpm (Sorval RC-5C Centrifuge, Thermo Scientific, Asheville, NC) for 20 min. Finally, the slurry was placed into a vacuum

oven at 70 °C for 24 h. Then, the nanocatalyst with 20 wt.% loading of PtRu mixed with carbon supported materials was obtained.

2.4. Characterization of PtRu nanocatalysts with different carbon supported materials

Phase structures and compositions of the PtRu nanocatalysts with different carbon supported materials were examined by XRD (Rigaku Corporation, Tokyo, Japan) using Cu Kα radiation ($\lambda = 1.54$ Å) and operating at 30 kV and 15 mA with a scan rate of 3°/min for 2θ in a range from 15° to 85°. The particle size of alloy nanoparticles was estimated using Debye–Scherrer's equation. SEM images were obtained at 5.0 keV on a Quanta 3D SEM (FEI, Hillsboro, OR). The morphologies of the nanocatalysts were studied using a Tecnai F30 STEM (FEI, Hillsboro, OR) and operated at 300 keV. The specimens for STEM analysis were prepared by ultrasonically suspending the nanocatalyst powders in ethanol. The suspension was then immediately dropped and dried on an ultrathin carbon supported 400 mesh copper grid (Ted Pella, Inc., Redding, CA) which was used for STEM examination.

2.5. Electrochemical measurements

Literatures suggested that metal nanoparticles-based sensor electrodes often gave increased current response and higher sensitivity and selectivity for H_2O_2 sensing (Dey and Raj, 2010; Chen et al., 2012b). Prior to experiments, PBS was deoxygenated with nitrogen gas. A glassy carbon electrode (GCE) was cleaned with acetone and ethanol in sequence, and then polished with 0.05 μm alumina powder. The GCE was then rinsed with DI water and sonicated for 10 min. In a typical H_2O_2 detection run, the bimetallic nanocatalyst with the carbon based substrate was placed on the surface of a rotating disk electrode for evaluation. One milligram of metal/carbon powder was dispersed in a 45 μL of ethanol and 5 μL of Nafion solution (15 wt.%), and then sonicated for 10 min to prepare the electrocatalyst. After sonication, 8.0 μL of the mixture was deposited onto the glassy carbon working electrode with a surface area of 0.196 cm^2 (Part no. AFE2M050GC, PINE Instrument Company, Grove City, PA). This thick film ink-coated electrode was dried under ambient condition for 3 min. A saturated calomel electrode (SCE) and a Pt mesh electrode (1 cm^2) were served as a reference and a counter electrode, respectively. The working electrode was operated at the rotational speed of 1000 rpm. The electrochemical titrations of various H_2O_2 in a PBS at pH = 7.4 with 0.15 M KCl as supporting electrolyte were carried out. A workstation (CHI 660C, CH Instrument, Inc., Austin, TX) was used for cyclic voltammetry and amperometry. Cyclic voltammetric studies were arranged over a voltage range of −0.2 V to +1.2 V versus the SCE with a voltage scan rate of 0.1 V/s.

In order to evaluate the ECSA of the nanocatalyst, the CO stripping measurement was conducted in a solution of 0.5 M H_2SO_4. The prepared process of nanocatalysts for the CO stripping measurement was identical to that for H_2O_2 detection as described above. Pure CO (99.5%) was then purged closed to the working electrode for 1 h with the electrode polarized at −0.15 V versus SCE. The CO adsorption time was found to be sufficient to reach the steady state. Afterwards, the dissolved CO was removed by bubbling Ar into the solution for 20 min, and the stripping voltammograms

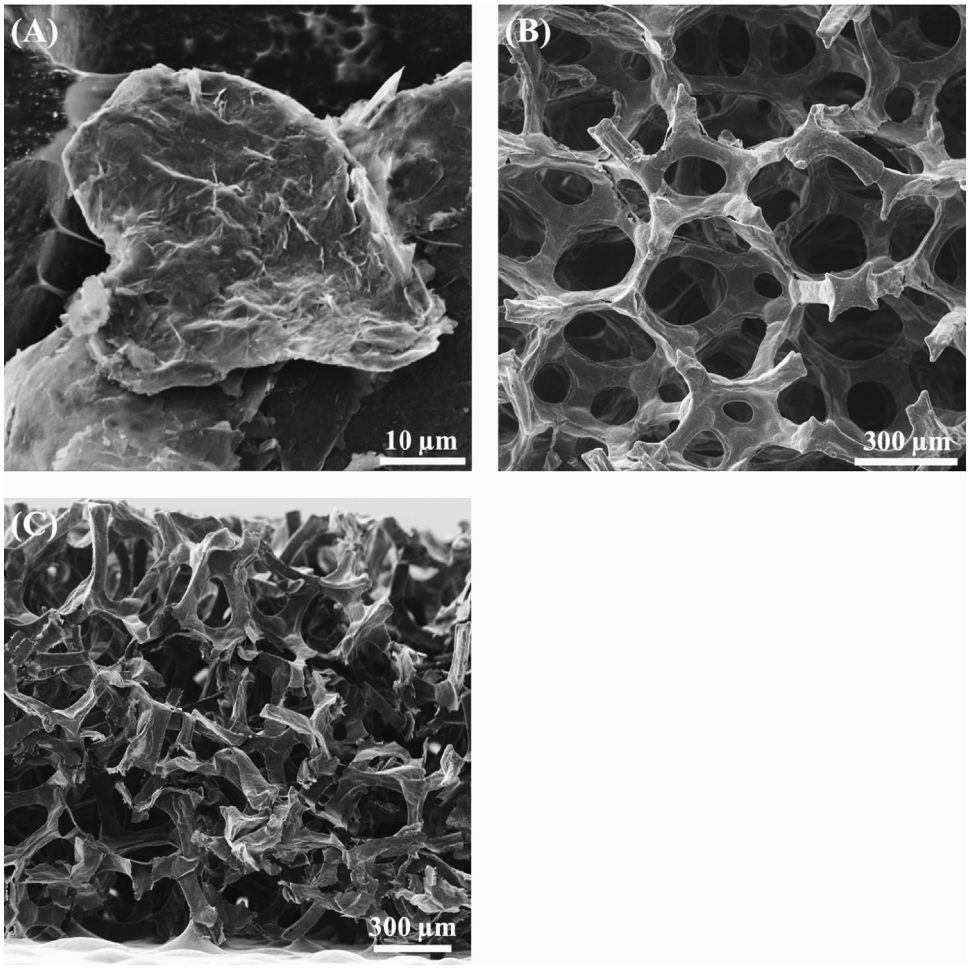

Fig. 1. SEM images of (A) pure commerical graphene, (B) pure graphene foam (plane view), (C) pure graphene foam (cross section).

were collected at a scan rate of 0.5 V/s. Two cyclic voltammmetries were recorded from −0.2 V to +1.2 V versus SCE. The first potential sweep was conducted to electro-oxidize the adsorbed CO and the second potential sweep was to verify the completeness of the CO oxidation.

3. Results and discussion

3.1. Physicochemical characterization of PtRu nanocatalysts with different carbon supported materials

The morphologies of the pure commercial graphene and 3D GF were characterized by SEM as shown in Fig. 1(A) and (B). The morphology was totally different between these two samples. Pure commercial graphene possessed a wrinkled and sheetlike structure. However, GF exhibited a macroporous structure with the pore diameter 50–250 μm. 3D GF showed a larger surface area comparing with the commercial graphene due to its macroporous structure. Moreover, 3D GF supplied a large number of active sites for adsorption of PtRu nanoparticles, and PtRu nanoparticles dispersed homogenously on the surface (Dong et al., 2012). GF also revealed an ultra-hollow internal structure with a high porosity based on the cross section of SEM (Fig. 1(C)). Supplementary information Fig. S1(A)–(D) shows the STEM images for the PtRu, PtRu/C, PtRu/graphene and PtRu/3D GF nanocatalysts, respectively. PtRu nanoparticles with relatively uniform dispersions were formed on the different carbon supported materials. In the STEM images of pure PtRu (Supplementary information Fig. S1(A)), an aggregation of nanoparticles was observed, because pure PtRu nanoparticles were not separated without carbon supported materials. Additionally, the PtRu nanoparticles were uniformly well-dispersed with Vulcan XC-72 carbon (Supplementary information Fig. S1(B)), and graphene (Supplementary information Fig. S1(C)) especially for the 3D GF (Supplementary information Fig. S1(D)) based on the STEM images. This was due to the availability of more surface area of the carbon supported materials, facilitating better dispersion of the PtRu nanoparticles. For Supplementary information Fig. S1(C) and (D), PtRu nanoparticles were dispersed onto the graphene sheets and GF, respectively. Both images displayed a slightly wrinkled morphology. Aksay et al. stated that this wrinkle was an important factor to prevent the aggregation of graphene and maintain high active surface area (McAllister et al., 2007; Kou et al., 2009). The STEM image of Supplementary information Fig. 1(D) showed a nanoporous structure providing the substrate for PtRu nanoparticles to adsorb on the flat layer and the scaffold. The average nanoparticle size of PtRu/3D GF nanocatalyst was smaller than with other carbon supported materials. The size difference and nanoparticle dispersion could be explained by the different specific surface areas of carbon supported materials and calculated based on the results of XRD.

Fig. 2 shows the XRD patterns of PtRu, PtRu/C, PtRu/graphene and PtRu/3D GF nanocatalysts. For pure Pt crystal, the peaks at 39.76°, 46.24°, 67.45°, and 81.28° were correspond to the (111), (200), (220) and (311) planes, respectively. These peaks indicated that Pt was presented in the face-centered cubic (fcc) structure (Zhang and Chan, 2003). The 2θ values of the (220) peaks for the PtRu, PtRu/C, PtRu/graphene and PtRu/3D GF nanocatalysts were observed at 67.92°, 67.52°, 67.96° and 67.48°, respectively. All of the peaks were slightly shifted to higher angles from pure Pt crystal, indicating as the evidence of alloying (Cong et al., 2012). The absence of the peaks associated with a typical hcp structure of pure Ru or RuO_2 in the XRD pattern suggested that Ru either formed alloys with Pt atoms or existed as oxides in the amorphous state (Prabhuram et al., 2006). The diffraction peak at 54.7° indicated the (004) plane of carbon

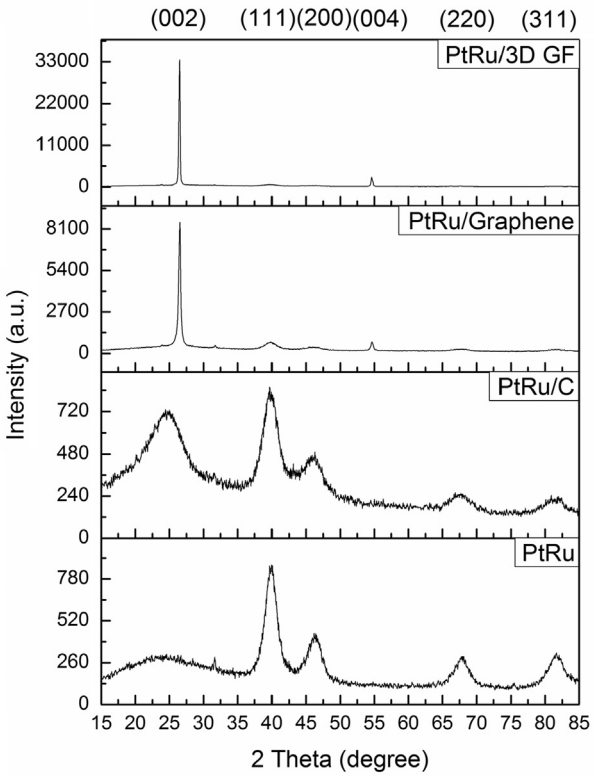

Fig. 2. X-ray diffraction patterns of PtRu-based nanocatalysts with different carbon supported materials.

support. This peak appeared when only high graphitization was achieved (Zhou et al., 2012). Also, the diffraction peak at around 26° observed in all the XRD patterns of the carbon supported nanocatalysts was due to the (002) plane of the hexagonal structure of carbon support. The existence of sharp diffraction peaks (002) demonstrated the crystalline nature of carbon support material. Carbon support material therefore acted as a good conductive substrate and influenced the crystalline nature of the Pt and PtRu nanoparticles being dispersed over the carbon material. In the case of PtRu/3D GF nanocatalyst, a very sharp peak appeared at the same 2θ value indicating the good crystalline nature and excellent conductivity of the GF.

The average particle size of the nanocatalyst was calculated from the Pt (220) diffraction peaks using Debye–Scherrer equation:

$$d = \frac{k\lambda}{\beta_{2\theta} \cos \theta_{\max}} \quad (3)$$

where k was a coefficient (0.9), λ was the wavelength of the X-ray (1.54 Å), β was the full width at half-maximum (FWHM) of the respective diffraction peak (rad), θ was the angle at the position of peak maximum (°).

The nanoparticle sizes of Pt calculated by the Debye–Scherrer equation were 7.07, 5.39, 4.24, and 3.51 nm for the PtRu, PtRu/C, PtRu/graphene and PtRu/3D GF nanocatalysts, respectively. In general, the nanoparticle size of Pt decreased when adding the carbon supported material during the preparation process, suggesting that the nanoparticle size of PtRu alloy in the nanocatalysts decreased with the addition of carbon supported material. Among the four nanocatalysts, the nanoparticle size for PtRu/3D GF nanocatalyst was the smallest, while that for PtRu nanocatalyst was the biggest. This large nanoparticle size of PtRu was probably due to agglomeration. This result indicated that PtRu/3D GF nanocatalyst had the largest surface area due to its smallest nanoparticle size among the four nanocatalysts. Thus, homogeneous distribution of PtRu nanoparticles

was obtained by adding the carbon supported materials which provided the large surface area. PtRu nanocatalysts with small nanoparticle sizes and a uniform distribution indicated that the active binding sites of itself increased enhancing the possibility to interact with H_2O_2.

3.2. Electrochemical characterization and performance

The electrochemical performances of PtRu nanocatalyst with different carbon supported materials were investigated by cyclic voltammetry (CV) using potassium ferricyanide (15 mM) and potassium ferrocyanide (15 mM) as the benchmark redox reactions for various modified electrodes. As shown in Fig. 3, the intensity of redox peak for pure PtRu nanocatalyst was low and the peak-to-peak potential separation ($\Delta E_p = E_{pa} - E_{pc}$) was 172 mV. In addition, the peak separations of the PtRu/C, PtRu/graphene and PtRu/3D GF nanocatalysts were 152, 155 and 166 mV, respectively. When glassy carbon electrode (GCE) was deposited with different carbon supported materials, the peak separation decreased and the redox peak current of $[Fe(CN)_6]^{3-/4-}$ increased substantially. The smaller peak-to-peak potential separation and the existence of sharp redox peaks current of $[Fe(CN)_6]^{3-/4-}$ demonstrated that the carbon supported materials improved the electron and mass transfer due to the increased surface area and lower electric resistance of nanosized PtRu particles. The smaller nanosized PtRu particles accelerated the electron-transfer kinetics. PtRu/3D GF specimen showed the best improvement in the anodic peak current (i_{pa}) and cathodic peak current (i_{pc}) by extending the three dimensional structure of GF. This result indicated that the carbon supported material provided the larger surface area, the electron and mass transfer rate would be accelerated due to the finer nanoparticle size and more uniform dispersion of PtRu nanocatalysts (Chen et al., 2012b). This performance also carried out by the STEM images and XRD results.

Enzymatic produced H_2O_2 shown in Eq. (1) was oxidized at an appropriate electrochemical potential. The oxidation current of the generated H_2O_2 quantified the concentration of analyte stoichiometrically. In order to verify the capability of this PtRu nanocatalyst for the detection of H_2O_2, experiment was firstly conducted measuring H_2O_2 in 0.1 M pH 7.4 PBS with 0.15 M KCl as a supporting electrolyte. The range of scanned potential was set between −0.2 V and +1.2 V versus SCE for six cycles with a voltage scan rate of 0.1 V/s. Supplementary information Fig. S2 compares the measured cyclic voltammogram of the 3rd and 4th cycles in PBS with and without 2 mM H_2O_2. A separable current appear at +0.2 V versus the SCE reference electrode demonstrating the ability of this PtRu nanocatalyst for the detection of H_2O_2 at that oxidation potential.

3.3. Electrochemical active surface area measurement

CO stripping voltammetry was applied to evaluate the ECSA of the nanocatalyst (Saha et al., 2007; Chetty et al., 2009). Supplementary information Fig. S3 shows the CO stripping voltammograms and the subsequent CV for the PtRu (Supplementary information Fig. S3(A)), PtRu/C (Supplementary information Fig. S3(B)), PtRu/graphene (Supplementary information Fig. S3(C)) and PtRu/3D GF (Supplementary information Fig. S3(D)) nanocatalysts in 0.5 M H_2SO_4 at a scan rate of 0.5 V/s. For all of the nanocatalysts, the first scan showed that the CO oxidation peaks were present at $E \approx 0.5$ V and no CO oxidation was observed in the second scan confirming the complete removal of the CO_{ads} species. The ECSA was estimated by using the following equation:

$$\mathrm{ECSA} = \frac{Q_{co}}{[\mathrm{Pt}] \times 420\ \mu\mathrm{C\ cm^{-2}}} \quad (4)$$

where Q_{co} represented the charge for the CO stripping (mC cm^{-2}), [Pt] was the platinum loading (mg cm^{-2}) in the electrode, and 420 μC cm^{-2} was the charge density which was required to oxidize a monolayer of CO. The relevant results were calculated to be 37.2 $m^2\ g^{-1}$, 54.2 $m^2\ g^{-1}$, 121.8 $m^2\ g^{-1}$ and 186.2 $m^2\ g^{-1}$ for the PtRu, PtRu/C, PtRu/graphene and PtRu/3D GF, respectively. It should be noted that the ECSA of the PtRu/3D GF nanocatalyst was higher than those of the other three nanocatalysts. The higher ECSA of PtRu/3D GF was due to the smaller size and better dispersion of the PtRu nanoparticles on GF. This observation was in agreement with the experimental results stated by XRD that PtRu/3D GF nanocatalyst had the largest surface area.

3.4. Amperometric measurement of H_2O_2

The performances of the PtRu nanocatalysts with different carbon supported materials were evaluated by the amperometric detections of H_2O_2. Fig. 4 shows the typical amperometric responses of the PtRu, PtRu/C, PtRu/graphene, and PtRu/3D GF nanocatalysts for continual additions of H_2O_2 to a stirred supporting electrolyte solution at an applied potential of +0.32 V versus SCE. This applied potential of +0.32 V versus SCE was selected to avoid the interference from AA and UA. The stable amperometric response was obtained and the responsive time was less than 10 s achieving 95%

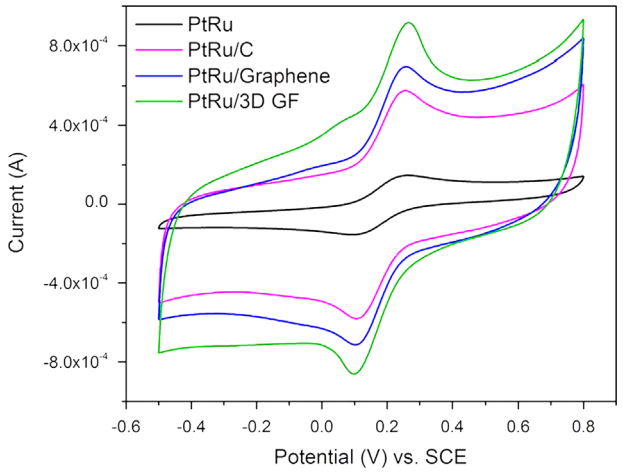

Fig. 3. Cyclic voltammograms of PtRu nanocatalysts with different carbon supported materials in 0.1 M PBS (pH=7.4) with 0.15 M KCl containing 15 mM each of $Fe(CN)_6^{3-}$ and $Fe(CN)_6^{4-}$.

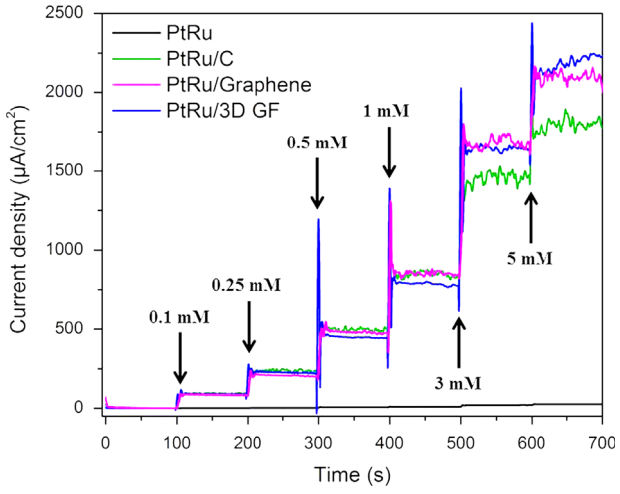

Fig. 4. Amperometric responses of PtRu nanocatalysts with different carbon supported materials obtained from successive additions of H_2O_2.

steady state current for the nanocatalyst with carbon supported materials. The fast response was due to the high electronic conductivity and good catalytic activity of PtRu nanoparticles with different carbon supported materials facilitated the electron transfer in the nanocomposite film. Moreover, the PtRu/3D GF nanocatalyst exhibited a larger current output (corresponding to time) than PtRu, PtRu/C and PtRu/graphene. In Supplementary information Fig. S4 the amperometric currents versus H_2O_2 concentrations were compared for the four nanocatalysts. The experimentally measured maximum detectable H_2O_2 concentration was found to be 5 mM with a signal-to-noise ratio of 3. This was the average of three successive measurements, corresponding to the same H_2O_2 concentration. PtRu/3D GF nanocatalyst showed the best performance when the concentration of H_2O_2 reached 5 mM. This result suggested that PtRu/3D GF nanocatalyst maintained good diffusion property because of the large surface area and high catalytic activity.

Fig. 5 shows time-dependent current of the PtRu/3D GF nanocatalyst for additions of H_2O_2 over a concentration range of 0.005–0.04 mM. The PtRu/3D GF amperometric sensor responded rapidly achieving 95% of the steady-state current within 10 s. As shown in Supplementary information Fig. S5, the calibration was linear over a H_2O_2 concentration range 0.005–0.02 mM: the linear regression equation was I (μA cm^{-2})=1023.1 (μA mM^{-1} cm^{-2})C (mM)+1.14 (μA cm^{-2}) with a coefficient of determination (R^2)=0.999. The

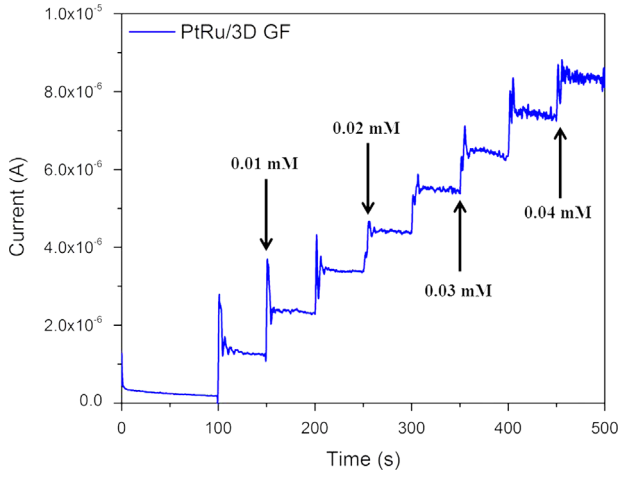

Fig. 5. Current versus time curve of the PtRu/3D GF for successive additions of H_2O_2.

sensitivity and the detection limit were 1023.1 μA mM^{-1} cm^{-2} and 0.04 μM, respectively. The detection limit was calculated based on the signal to noise ratio (S/N=3). PtRu/3D GF nanocatalyst showed the highest sensitivity and the best of limit of detection (LOD) among four samples, following by PtRu/graphene, PtRu/C, and PtRu in order. The high LOD of the PtRu/3D GF nanocatalyst was attributed to the nanocatalyst having a high electrocatalytic activity. Additionally, the stability of this nanocatalyst reduced the interference of background current achieving the higher LOD. The performance of PtRu nanocatalysts with different carbon supported materials were compared with other nanocatalysts as shown in Table 1, including applied potential, linear range, sensitivity and detection limit. PtRu/3D GF nanocatalyst showed the excellent performance which was contributed to the large surface area and excellent electrical conductivity of GF.

3.5. Interference tests

The interference from physiological species such as ascorbic acid (AA) and uric acid (UA) was always a concern for H_2O_2 based electrochemical biosensor. The concentrations of AA and UA in human blood were 0.125 mM and 0.33 mM, respectively (You et al., 2012). Responses to the successive addition of 1.0 mM H_2O_2, 0.15 mM AA, and 0.5 mM UA were measured at +0.32 V versus SCE, as shown in Supplementary information Fig. S6. The negligible effects of the interferences on the H_2O_2 response indicated the high selectivity of the PtRu/3D GF nanocatalyst. The high selectivity could be attributed to a relative low potential applying for H_2O_2 detection minimizing the responses of common interfering species.

3.6. Stability and durability of the PtRu/3D GF nanocatalyst

The stability of the PtRu/3D GF nanocatalyst had been investigated through the amperometric response to 0.04 mM H_2O_2 at +0.32 V versus SCE in 0.1 M PBS (pH=7.4) with 0.15 M KCl. In a series of eight successive measurements, 0.005 mM H_2O_2 was measured continuously, and a good stability with a relative standard deviation (RSD) of 1.54% was obtained from three different electrodes prepared under the same conditions. The results showed that the PtRu/3D GF nanocatalyst had satisfactory stability as shown in Supplementary information Fig. S7. For durability evaluation, the PtRu/3D GF electrode was stored in 0.1 M PBS (pH=7.4) with 0.15 M KCl at room temperature (25 °C) when not in use. The PtRu/3D GF electrode was then investigated through the amperometric response to 5 mM H_2O_2 at +0.32 V versus SCE in 0.1 M PBS (pH=7.4) with

Table 1
A comparison of the performance using Pt based nanoparticles toward the H_2O_2 detection.

Catalyst	Applied potential (V)		Linear range (mM)	Sensitivity (μA mM^{-1} cm^{-2})	LOD (μM)	Reference
Pt/CNT	−0.1	(Ag/AgCl)	5×10^{-3}–25	140	1.5	Wen et al. (2009)
Pt/MWCNT	+0.7	(Ag/AgCl)	Up to 2.5	3847	0.025	Male et al. (2007)
Pt/t-MWCNT/PDDA[a]	−0.1	(Ag/AgCl)	1×10^{-3}–8	481.3	0.27	You et al. (2012)
Pt/t-GO/PDDA[b]	−0.1	(Ag/AgCl)	1×10^{-3}–5	353.9	0.65	You et al. (2012)
PtIr/MWCNT	+0.25	(SCE)	2.5×10^{-3}–0.075	58.8	2.5	Chen et al. (2012b)
PtPd/MWCNT	+0.25	(SCE)	2.5×10^{-3}–0.125	414.8	1.2	Chen et al. (2012b)
Nanoporous PtCu/C	+0.3	(Ag/AgCl)	0–4	69.4	12.2	Janyasupab et al. (2013)
Nanoporous PtNi/C	+0.3	(Ag/AgCl)	0–2	208.5	31.5	Janyasupab et al. (2013)
Nanoporous PtPd/C	+0.3	(Ag/AgCl)	0–3	239.8	114	Janyasupab et al. (2013)
Nanoporous PtRh/C	+0.3	(Ag/AgCl)	0–2	839.9	34.8	Janyasupab et al. (2013)
PtRu	+0.32	(SCE)	0–0.02	22.2	0.817	This work
PtRu/C	+0.32	(SCE)	0–0.02	791.5	0.379	This work
PtRu/graphene	+0.32	(SCE)	0–0.02	795.4	0.355	This work
PtRu/3D GF	+0.32	(SCE)	0–0.02	1023.1	0.04	This work

[a] Pt/t-MWCNT/PDDA represented a Pt/thiolated-MWCNT/poly-(diallyldimethylammonium chloride).
[b] Pt/t-GO/PDDA represented a Pt/thiolated-graphene oxide/poly-(diallyldimethylammonium chloride).

0.15 M KCl. The results showed that the PtRu/3D GF electrode remained at 96.5% of its original response after 7 days, 94.1% after 14 days, and 93.4% after 21 days, suggesting that the good stability and durability of the PtRu/3D GF nanocatalyst for H_2O_2 detection. This result demonstrated that the three dimensional structure facilitated the electron and mass transfer due to the increased surface area and high conductivity of nanosized PtRu particles.

4. Conclusions

The measurement of H_2O_2 based amperometric biosensors was often inaccurately due to the low sensitivity and low LOD toward the H_2O_2 detection. Converting bimetallic nanoparticles into 3D porous structure enhanced the active surface area and increased the effective transport in the reaction. In this study, PtRu bimetallic nanoparticles with 3D GF nanocatalyst for H_2O_2 detection was designed. 3D GF demonstrated to be as a good platform to incorporate with PtRu bimetallic nanoparticles for biosensing. PtRu/3D GF nanocatalyst exhibited a good performance toward electrochemical oxidation of H_2O_2 without any additional mediator or enzyme possessing a high sensitivity (1023.1 $\mu A\ mM^{-1}\ cm^{-2}$) and a low detection limit (0.04 μM). 3D GF improved the availability ECSA of nanocatalyst for electron transfer and also provided high mass transport of reactants to the nanocatalyst. The increased active binding sites of PtRu/3D GF nanocatalyst showed a higher possibility to interact with H_2O_2, enhancing the catalytic activity of the H_2O_2 detection.

Acknowledgments

This study was supported by the DOD-Air Force Office of Scientific Research – MURI 2011-microfabrication. Technical assistance from the staff of Electronics Design Center of Case Western Reserve University was gratefully acknowledged.

Appendix A. Supporting information

Supplementary data associated with this article can be found in the online version at http://dx.doi.org/10.1016/j.bios.2013.08.025.

References

Alayoglu, S., Nilekar, A.U., Mavrikakis, M., Eichhorn, B., 2008. Nature Materials 7, 333–338.
Bi, H., Huang, F., Liang, J., Tang, Y., Lü, X., Xie, X., Jiang, M., 2011. Journal of Materials Chemistry 21, 17366–17370.
Bligaard, T., Nørskov, J.K., Dahl, S., Matthiesen, J., Christensen, C.H., Sehested, J., 2004. Journal of Catalysis 224, 206–217.
Chakraborty, S., Raj, C.R., 2009. Biosensors & Bioelectronics 24, 3264–3268.
Chang, Y.W., Liu, C.W., Wei, Y.C., Wang, K.W., 2009. Electrochemistry Communications 11, 2161–2164.
Chen, Z., Ren, W., Gao, L., Liu, B., Pei, S., Cheng, H.M., 2011. Nature Materials 10, 424–428.
Chen, K.J., Lee, C.F., Rick, J., Wang, S.H., Liu, C.C., Hwang, B.J., 2012a. Biosensors & Bioelectronics 33, 75–81.
Chen, K.J., Pillai, K.C., Rick, J., Pan, C.J., Wang, S.H., Liu, C.C., Hwang, B.J., 2012b. Biosensors & Bioelectronics 33, 120–127.
Chetty, R., Kundu, S., Xia, W., Bron, M., Schuhmann, W., Chirila, V., Brandle, W., Reinecke, T., Muhler, M., 2009. Electrochimica Acta 54, 4208–4215.
Cong, H.P., Ren, X.C., Yu, S.H., 2012. ChemCatChem 4, 1555–1559.
Dai, L., Chang, D.W., Baek, J.B., Lu, W., 2012. Small 8, 1130–1166.
Dong, X., Wang, X., Wang, L., Song, H., Zhang, H., Huang, W., Chen, P., 2012. ACS Applied Materials and Interfaces 4, 3129–3133.
Dey, R.S., Raj, C.R., 2010. Journal of Physical Chemistry C 114, 21427–21433.
Evans, S.A.G., Elliott, J.M., Andrews, L.M., Bartlett, P.N., Doyle, P.J., Denuault, G., 2002. Analytical Chemistry 74, 1322–1326.
Ge, Q., Desai, S., Neurock, M., Kourtakis, K., 2001. Journal of Physical Chemistry 105, 9533–9536.
Gong, K., Yu, P., Su, L., Xiong, S., Mao, L., 2007. Journal of Physical Chemistry C 111, 1882–1887.
Greeley, J., Rossmeisl, J., Hellman, A., Nørskov, J.K., 2007. Zeitschrift für Physikalische Chemie 221, 1209–1220.
Gsell, M., Jakob, P., Menzel, D., 1998. Science 280, 717–720.
Guascito, M.R., Filippo, E., Malitesta, C., Manno, D., Serra, A., Turco, A., 2008. Biosensors & Bioelectronics 24, 1057–1063.
Guo, Y.G., Hu, J.S., Wan, L.J., 2008. Advanced Materials 20, 2878–2887.
Huang, X., Qian, K., Yang, J., Zhang, J., Li, L., Yu, C., Zhao, D., 2012. Advanced Materials 24, 4419–4423.
Jakob, P., Gsell, M., Menzel, D., 2001. Journal of Chemical Physics 114, 10075–10085.
Janyasupab, M., Liu, C.W., Zhang, Y., Wang, K.W., Liu, C.C., 2013. Sensors Actuators B 179, 209–214.
Karam, P., Halaoui, L.I., 2008. Analytical Chemistry 80, 5441–5448.
Kou, R., Shao, Y., Wang, D., Engelhard, M.H., Kwak, J.H., Wang, J., Viswanathan, V.V., Wang, C., Lin, Y., Wang, Y., Aksay, I.A., Liu, J., 2009. Electrochemistry Communications 11, 954–957.
Kua, J., Goddard III, W.A., 1999. Journal of the American Chemical Society 121, 10928–10941.
Lee, S.H., Kim, H.W., Hwang, J.O., Lee, W.J., Kwon, J., Bielawski, C.W., Ruoff, R.S., Kim, S.O., 2010. Angewandte Chemie International Edition 49, 10084–10088.
Lischka, M., Mosch, C., Groß, A., 2007. Electrochimica Acta 52, 2219–2228.
Liu, J., Cao, G., Yang, Z., Wang, D., Dubois, D., Zhou, X., Graff, G.L., Pederson, L.R., Zhang, J.G., 2008. ChemSusChem 1, 676–697.
Liu, C.W., Wei, Y.C., Wang, K.W., 2011. Journal of Physical Chemistry C 115, 8702–8708.
Loh, K.P., Bao, Q., Ang, P.K., Yang, J., 2010. Journal of Materials Chemistry 20, 2277–2289.
Male, K.B., Hrapovic, S., Luong, J.H.T., 2007. Analyst 132, 1254–1261.
Mattevi, C., Eda, G., Agnoli, S., Miller, S., Mkhoyan, K.A., Celok, O., Mastrogiovanni, D., Granozzi, G., Garfunkel, E., Chhowalla, M., 2009. Advanced Functional Materials 19, 2577–2583.
McAllister, M.J., Li, J., Adamson, D.H., Schniepp, H.C., Abdala, A.A., Liu, J., 2007. Chemistry of Materials 19, 4396–4404.
McLamore, E.S., Shi, J., Jaroch, D., Claussen, J.C., Uchida, A., Jiang, Y., Zhang, W., Donkin, S.S., Banks, M.K., Buhman, K.K., Teegarden, D., Rickus, J.L., Porterfield, D. M., 2011. Biosensors & Bioelectronics 26, 2237–2245.
Prabhuram, J., Zhao, T.S., Tang, Z.K., Chen, R., Liang, Z.X., 2006. Journal of Physical Chemistry B 110, 5245–5252.
Privett, B.J., Shin, J.H., Schoenfisch, M.H., 2008. Analytical Chemistry 80, 4499–4517.
Rolison, D.R., Long, J.W., Lytle, J.C., Fischer, A.E., Rhodes, C.P., McEvoy, T.M., Bourg, M. E., Lubers, A.M., 2009. Chemical Society Reviews 38, 226–252.
Saha, M.S., Li, R., Sun, X., 2007. Electrochemistry Communications 9, 2229–2234.
Shi, J., Cha, T.G., Claussen, J.C., Diggs, A.R., Choi, J.H., Porterfield, D.M., 2011. Analyst 136, 4916–4924.
Shi, J., Zhang, H., Snyder, A., Wang, M.X., Xie, J., Porterfield, D.M., Stanciu, L.A., 2012. Biosensors & Bioelectronics 38, 314–320.
Si, P., Dong, X.C., Chen, P., Kim, D.H., 2013. Journal of Materials Chemistry B 1, 110–115.
Singh, E., Chen, Z., Houshmand, F., Ren, W., Peles, Y., Cheng, H.M., Koratkar, N., 2013. Small 1, 75–80.
Sundaram, R.S., Steiner, M., Chiu, H.Y., Engel, M., Bol, A.A., Krupke, R., Burghard, M., Kern, K., Avouris, P., 2011. Nano Letters 11, 3833–3837.
Wang, H., Yang, Y., Liang, Y., Robinson, J.T., Li, Y., Jackson, A., Cui, Y., Dai, H., 2011. Nano Letters 11, 2644–2647.
Wei, Y.C., Liu, C.W., Chang, W.J., Wang, K.W., 2011. Journal of Alloys and Compounds 509, 535–541.
Wen, Z., Ci, S., Li, J., 2009. Journal of Physical Chemistry C 113, 13482–13487.
Wu, P., Shao, Q., Hu, Y.J., Jin, J., Yin, Y.J., Zhang, H., Cai, C.X., 2010. Electrochimica Acta 55, 8606–8614.
Yin, S., Zhang, Y., Kong, J., Zou, C., Li, C.M., Lu, X., Ma, J., Boey, F.Y.C., Chen, X., 2011. ACS Nano 5, 3831–3838.
You, J.M., Kim, D., Jeon, S., 2012. Electrochimica Acta 65, 288–293.
Zhang, X., Chan, K.Y., 2003. Chemistry of Materials 15, 451–459.
Zhou, Q., Zhao, Z., Zhang, Y., Meng, B., Zhou, A., Qiu, J., 2012. Energy Fuels 26, 5186–5192.